

Economical Pt-Free Catalysts for Counter Electrodes of Dye-Sensitized Solar Cells

Mingxing Wu,^{†,‡} Xiao Lin,^{†,‡} Yudi Wang,^{†,‡} Liang Wang,^{†,‡} Wei Guo,^{†,‡} Daidi Qi,^{†,‡} Xiaojun Peng,^{*,†} Anders Hagfeldt,[§] Michael Grätzel,^{||} and Tingli Ma^{*,†,‡}

[†]State Key Laboratory of Fine Chemicals, Dalian University of Technology, No. 2 Linggong Road, Ganjingzi District, Dalian City, Liaoning Province, P. R. China 116024

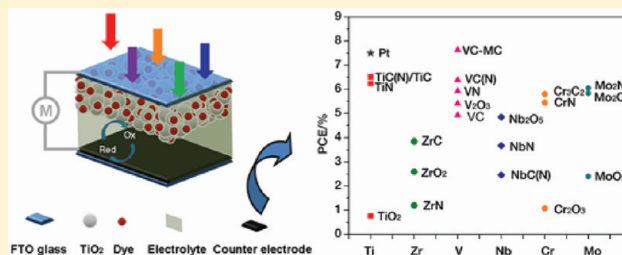
[‡]School of Chemical Engineering, Dalian University of Technology, No. 2 Linggong Road, Ganjingzi District, Dalian City, Liaoning Province, P. R. China 116024

[§]Department of Physical and Analytical Chemistry, Uppsala University, Box 259, SE-751 05 Uppsala, Sweden

^{||}Laboratory for Photonics and Interfaces, Institute of Chemical Sciences and Engineering, Swiss Federal Institute of Technology, CH 1015 Lausanne, Switzerland

Supporting Information

ABSTRACT: Three classes (carbides, nitrides and oxides) of nanoscaled early-transition-metal catalysts have been proposed to replace the expensive Pt catalyst as counter electrodes (CEs) in dye-sensitized solar cells (DSCs). Of these catalysts, Cr₃C₂, CrN, VC(N), VN, TiC, TiC(N), TiN, and V₂O₃ all showed excellent catalytic activity for the reduction of I₃[−] to I[−] in the electrolyte. Further, VC embedded in mesoporous carbon (VC-MC) was prepared through in situ synthesis. The I₃[−]/I[−] DSC based on the VC-MC CE reached a high power conversion efficiency (PCE) of 7.63%, comparable to the photovoltaic performance of the DSC using a Pt CE (7.50%). In addition, the carbide catalysts demonstrated catalytic activity higher than that of Pt for the regeneration of a new organic redox couple of T₂/T[−]. The T₂/T[−] DSCs using TiC and VC-MC CEs showed PCEs of 4.96 and 5.15%, much higher than that of the DSC using a Pt CE (3.66%). This work expands the list of potential CE catalysts, which can help reduce the cost of DSCs and thereby encourage their fundamental research and commercial application.



INTRODUCTION

Dye-sensitized solar cells (DSCs) demonstrate specific advantages over other photovoltaic devices, namely, simple fabrication procedures, environmental friendliness, transparency, and good plasticity.^{1–3} The counter electrode (CE), a crucial component of DSCs, performs two critical functions: it collects the electrons flowing from the external circuit and catalyzes the reduction of I₃[−] to I[−], thereby realizing the regeneration of the sensitizer. Although Pt deposited on fluorine-doped tin oxide (FTO) conductive glass is an effective CE for DSCs, the limited availability and high cost of Pt have restricted further development of DSCs.^{4–7} In addition, we have found that Pt is not suitable for the regeneration of new organic redox couples, such as di-5-(1-methyltetrazole) disulfide/5-mercapto-1-methyltetrazole N-tetramethylammonium salt (T₂/T[−]).⁸ It is urgent to develop new CE catalysts for both the traditional redox couple (I₃[−]/I[−]) and new redox couples (T₂/T[−], Co³⁺/Co²⁺).^{9–11} An alternative is to replace Pt with an economical catalyst that is endowed with both high catalytic activity and ready availability.¹² In previous studies, carbon materials and organic polymers were proposed for use as CE catalysts.^{13–17} More recently, several inorganic

compounds were introduced into DSCs as CE catalysts, such as CoS, NiS and NiN.^{18–20} However, the fact remains that there are few alternatives to replace the expensive Pt in fabricating economical, highly efficient DSCs. It has been established that early-transition-metal carbides (TMCs), nitrides (TMNs), and oxides (TMOs) have a number of strengths, including the durability of the covalent solid, the high melting temperatures of the ionic crystals, and electrical and thermal conductivities of the transition metals, although the most important aspect remains the Pt-like catalytic activity of these compounds.^{21,22} To date, TMCs and TMNs have been applied in the fields of space communication,²³ hydrogen oxidation,²⁴ and methanol oxidation,²⁵ whereas TMOs have been applied in gas sensors and field emitters.^{26,27} Nevertheless, few reports have focused on the application of TMCs, TMNs, or TMOs in DSC systems. Recently, we and another group developed economical tungsten carbide and tungsten oxide for use as the counter electrodes in DSC systems, and they showed excellent catalytic activity.^{28–30}

Received: October 14, 2011

The aim of this work was to synthesize a list of TMCs, TMNs, and TMOs and apply them in DSC systems as CE catalysts to replace the expensive Pt for the regeneration of the I_3^-/I^- and T_2/T^- redox couples. According to the urea-metal route, metal chloride was dissolved in ethanol to form the metal orthoester. Next, various amounts of urea were added to the metal orthoester, producing a gel-like urea-metal precursor. After the precursor was sintered, the target oxides, nitrides, and carbides were synthesized. The carbides and nitrides obtained using the soft urea-metal route are usually of high purity (>99.5% wt %), and the products require no preliminary treatments or further purification. In this work, we synthesized three classes of nanoscaled catalysts via this method, including TMCs (Cr_3C_2 , N-doped VC [VC(N)], N-doped TiC [TiC(N)], Mo_2C , and N-doped NbC [NbC(N)]), TMNs (CrN, VN, TiN, MoN, and NbN), and TMOs (Cr_2O_3 , V_2O_5 , TiO_2 , MoO_3 , Nb_2O_5 , and ZrO_2). Commercial TiC, VC, ZrC, and ZrN were used to ensure a systematic investigation of catalytic properties of these carbides, nitrides, and oxides as CE catalysts in DSCs. Cyclic voltammetry (CV), electrochemical impedance spectroscopy (EIS), and Tafel polarization measurements were applied to investigate the catalytic activities of these materials. With the exceptions of NbC, NbN, ZrN, TiO_2 , and Cr_2O_3 , all of the materials showed higher catalytic activity for I_3^- reduction in the DSC systems. In addition, the catalytic activity was improved by combining materials with high catalytic activity (VC) and electrical conductivity (mesoporous carbon, MC) into one composite material (VC-MC). Furthermore, Cr_3C_2 , TiC, VC, and VC-MC showed excellent catalytic behavior superior to that of Pt for the regeneration of the T_2/T^- redox couple.

■ EXPERIMENTAL SECTION

Materials. Ethanol was purchased from Kermel (Tianjin, China) and distilled before use. The metal chlorides involved in this work ($TiCl_4$, $ZrCl_4$, $NbCl_5$, $CrCl_3 \cdot 6H_2O$, and $MoCl_5$) were purchased from Aladdin (Shanghai, China). $VOCl_3$ was purchased from Aldrich. Urea, polyethylene-poly(propylene glycol) (F127), resorcinol, and formaldehyde all were purchased from Aladdin as well. ZrN was purchased from Alfa, and TiC, VC, and ZrC were purchased from Aladdin.

Synthesis of TMCs, TMNs, and TMOs. In the case of carbides, nitrides, and oxides, metal chlorides were used as metal precursors, ethanol (or urea) was used as the oxygen source, and urea could be used as either the carbon or nitrogen source depending on the urea/metal chloride molar ratio (nitrogen source at low urea/metal ratios and carbon source at high ratios). As an example, for Cr derivatives, as the urea/ $CrCl_3 \cdot 6H_2O$ molar ratio increased from 0 to 12 (denoted as Cr-Rx, $x = 0, 1, 3, 5, 7, 9, 12$, respectively), the metal precursor was transformed to Cr_2O_3 (Cr-R0), then to CrN (Cr-R5), and finally to Cr_3C_2 (Cr-R12). In detail, $CrCl_3 \cdot 6H_2O$ (2.67 g) was dissolved in 9 mL of ethanol and stirred for 2 h, and a dark-green solution was obtained. The specified amount of urea [0 (0), 1 (0.60), 3 (1.80), 5 (3.00), 7 (4.20), 9 (5.40), or 12 equiv (7.20 g)] was then added to the solution, which was stirred for 2 h until the urea dissolved completely. The color of the solution gradually turned from dark-green to purple. Next, the solution was heated at 120 °C to remove the residual ethanol, and then the intermediates were sintered at 800 or 1100 °C for 3 or 5 h under a N_2 atmosphere to afford pure Cr_2O_3 ($x = 0$, 800 °C, 3 h), CrN ($x \geq 5$, 800 °C, 3 h), or Cr_3C_2 ($x = 12$, 1100 °C, 5 h), respectively.

Synthesis of VC Embedded in MC (VC-MC). F127 (2.50 g) was added to ethanol (30 mL) and stirred until the F127 was completely dissolved. Resorcinol (1.65 g) and ethylic acid (0.40 g) were then added to the solution, which was stirred for 30 min. Next, 0.50 g of $VOCl_3$ was added to the solution, which was then stirred for ~3 h. This was followed by addition of formaldehyde (37 wt %, 3 mL) to the solution. The solution was allowed to stand in the dark for ~2 weeks

to allow the phenolic resin to form. The solution was cured at 80 °C for 3 days until a gel was obtained. Next, the gel was thermally decomposed at 1100 °C under a N_2 atmosphere for 5 h, affording VC-MC.

Cell Fabrication. A 8 μ m thick layer of 20 nm sized TiO_2 particles (Ti-Nanoxide D, Solaronix SA, Aubonne, Switzerland) sensitized with N719 dye (Solaronix) was used as the photoanode. Two kinds of redox couples were used in this research. The first was I_3^-/I^- . The I_3^-/I^- electrolyte contained 0.06 M LiI, 0.6 M 1-butyl-3-methylimidazolium iodide, 0.03 M I_2 , 0.5 M 4-*tert*-butylpyridine (TBP), and 0.1 M guanidinium thiocyanate in acetonitrile. The second was T_2/T^- , which was prepared according to the procedure reported previously.⁹ The T_2/T^- electrolyte contained 0.4 M $Me_4N^+T^-$, 0.4 M di-5-(1-methyltetrazole) disulfide (T_2), 0.05 M $LiClO_4$, and 0.5 M TBP in 6:4 (v/v) acetonitrile/ethylene carbonate. The CE was prepared as follows: 200 mg of the material (carbide, nitride, or oxide) was dispersed in 4 mL of isopropanol. The solution was then ultrasonically dispersed for 30 min, and the pastes for spraying were obtained. The prepared pastes were sprayed onto FTO glass with an air brush (spray gun). The catalyst layer thickness was controlled by the amount of paste used. Subsequently, the FTO glass coated with various pastes was sintered under a N_2 atmosphere at 500 °C for 30 min while the CEs were prepared. The Pt CE was prepared using the procedure in our previous works.⁵ The DSCs were fabricated with a photoanode, a counter electrode, and an electrolyte. The active area of the DSCs was 0.16 cm². Symmetrical cells with an active area of 0.35 cm² were fabricated with two identical CEs clipping the electrolyte. The cells were sealed with a hot-melt Surlyn film.

Measurements. X-ray diffraction (XRD) measurements were carried out using an automatic X-ray powder diffractometer (D/Max 2400, Rigaku). The surface morphologies of the nitride, carbide, and oxide powders were characterized by scanning electron microscopy (SEM) (S-4800 FEI, Hitachi) and transmission electron microscopy (TEM) (G² Spirit, Tecnai). The TiC film thickness was tested by SEM (Quanta 450, FEI). CV measurements were conducted in a three-electrode system in an argon-purged electrolyte solution at a scan rate of 10 mV s⁻¹ using an electrochemical analyzer (CHI630, Chenhua, Shanghai). Pt served as the CE, and Ag/Ag⁺ served as the reference electrode. The I_3^-/I^- electrolyte contained 0.1 M $LiClO_4$, 10 mM LiI, and 1 mM I_2 in acetonitrile. The T_2/T^- electrolyte contained 100 mM $Me_4N^+T^-$, 10 mM T_2 , and 0.2 M $LiClO_4$ in acetonitrile. The photocurrent-voltage performance of the DSCs was tested under simulated AM 1.5 illumination ($I = 100$ mW cm⁻², PEC-L15, Peccell, Yokohama, Japan) with a digital source meter (Keithley 2601, Cleveland, OH). EIS experiments were characterized with symmetrical cells in the dark using a computer-controlled potentiostat (Zennium Zahner, Kronach, Germany). The measured frequency ranged from 100 mHz to 1 MHz. The amplitude of the alternating current was set at 10 mV. Tafel polarization measurements were carried out with an electrochemical workstation system (CHI630, Chenhua, Shanghai) in a symmetrical dummy cell. The scan rate was 10 mV s⁻¹.

■ RESULTS AND DISCUSSION

Characterization of the As-Prepared Carbides, Nitrides, and Oxides by XRD and SEM. As shown in Figure 1 and Table S1 in the Supporting Information, pure Cr_2O_3 , CrN, and Cr_3C_2 were synthesized merely by adjusting the urea/metal chloride molar ratio (Cr-Rx, $x = 0, 1, 3, 5, 7, 9, 12$), the sintering temperature, and the sintering time. When no urea was added (Cr-R0) and the precursor was sintered at 800 °C for 3 h, Cr_2O_3 was obtained. As shown in Figure 1, the diffraction peaks at 24.48, 33.56, 36.12, 41.44, 44.17, 50.26, 54.86, 57.08, 63.4, 65.06, 72.86, 76.8, 79.16, 80.17, 82.06, 84.26, and 86.46° can be assigned to the [012], [104], [110], [113], [202], [024], [116], [111], [214], [300], [1010], [220], [306], [223], [312], [0210], and [134] crystal planes, respectively, of Cr_2O_3 (no. 38-1479, PDF-2 Database). This means that ethanol served as the oxygen source in the oxide formation

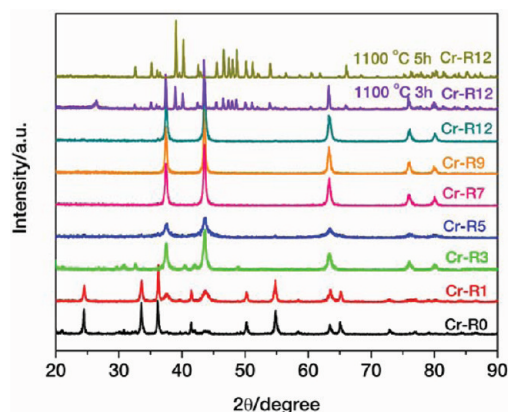


Figure 1. XRD patterns of the as-synthesized Cr_2O_3 , CrN, and Cr_3C_2 . Cr-R0, Cr_2O_3 ; Cr-R1, $\text{Cr}_2\text{O}_3/\text{CrN}$; Cr-R3, CrN with few impurities; Cr-R5, -R7, -R9, -R12, CrN (sintered at 800 °C for 3 h); Cr-R12 sintered at 1100 °C for 3 h, $\text{Cr}_3\text{C}_2/\text{CrN}$; Cr-R12 sintered at 1100 °C for 5 h, Cr_3C_2 .

process. When 1 equiv of urea was added, a $\text{Cr}_2\text{O}_3/\text{CrN}$ composite was obtained. As the urea/metal molar ratio reached 3, CrN with few impurities was obtained. Pure CrN was obtained for Cr-R5, -R7, -R9, and -R12 at a sintering temperature of 800 °C for 3 h. The diffraction peaks at 37.54, 43.60, 63.24, 76.14, and 80.08° can be assigned to the [111], [200], [220], [311], and [222] crystal planes, respectively, of CrN (no. 65-2899, PDF-2 Database). In the case of Cr-R12, when the sintering temperature was increased to 1100 °C for 3 h, an intermediate product of $\text{Cr}_3\text{C}_2/\text{CrN}$ was obtained. When the sintering time was prolonged to 5 h, pure Cr_3C_2 was synthesized successfully. The diffraction peaks at 32.59, 35.18, 36.07, 36.52, 39.04, 39.59, 40.21, 42.58, 42.95, 45.52, 46.59, 47.42, 48.02, 48.69, 50.13, 51.19, 52.16, 53.98, 55.30, 56.46, 58.65, 60.46, 61.86, 64.82, 66.03, 68.34, 70.96, 73.93, 75.18, 76.26, 77.88, 78.84, 79.74, 80.23, 81.44, 81.77, 83.06, 83.88, 85.16, 86.47, 87.28, 88.86, and 89.70° can be assigned to the [011], [140], [220], [111], [121], [031], [230], [150], [131], [240], [211], [060], [141], [221], [310], [051], [231], [151], [330], [241], [170], [311], [251], [350], [002], [410], [360], [351], [271], [181], [370], [421], [361], [232], [431], [152], [281], [242], [062], [1100], [312], [510], and [451] crystal planes, respectively, of Cr_3C_2 (no. 35-0804, PDF-2 Database). This is the first time that Cr_3C_2 has been prepared by the urea–metal. Thus, the urea–metal route is a fast, inexpensive way to obtain nanoscaled, well-crystallized, high-purity TMCs, TMNs, and TMOs. This directly provides the feasibility of reducing the cost of DSCs by using these cheap materials as CE catalysts in place of expensive Pt CE.

Under the same conditions, V_2O_3 , VN, VC(N), TiO_2 , TiN, and TiC(N) were prepared successfully. The corresponding XRD parameters are summarized in Figure 2. In the case of the oxides (i.e., without addition of urea), TiO_2 and V_2O_3 were obtained. For urea/metal chloride molar ratio up to 5 (R5), TiN and VN were produced. The sintering temperature for preparing oxides and nitrides was 800 °C. According to the method for synthesizing Cr_3C_2 , we increased the sintering temperature to 1100 °C to prepare the expected VC and TiC. However, the XRD patterns of VN and VC (TiN and TiC) were too similar to distinguish them. Furthermore, XPS measurements carried out for the expected TiC showed a typical N–Ti bonding energy peak at ~400 eV (Figure S1 in

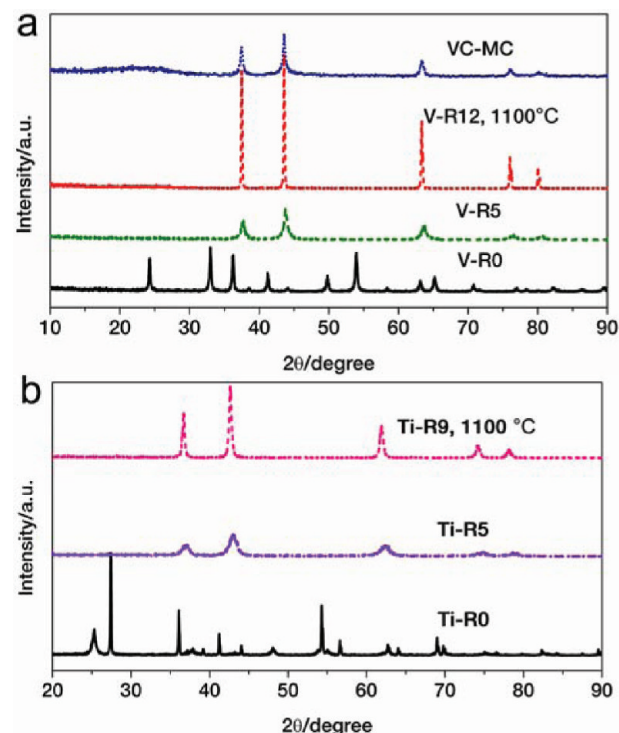


Figure 2. (a) XRD patterns of V_2O_3 (V-R0), VN (V-R5), VC(N) (V-R12), and VC–MC. (b) XRD patterns of TiO_2 (Ti-R0), TiN (Ti-R5), and TiC(N) (Ti-R12).

the Supporting Information). This means that VC(N) and TiC(N) were prepared at high urea concentration and high sintering temperature. The results are in good agreement with previous research.³¹ According to previous studies, at high urea/metal chloride molar ratios, the nitrogen and oxygen were removed from the metal–urea gel through the formation of NO_x as the sintering temperature increased, while the carbon remained unchanged. This indicates that metal–C chemical bonds are built in the process of carbide formation. It is worth acknowledging that no traces of side products (such as oxides and amorphous C) were observed by either XRD or SEM/TEM characterization in the as-prepared nitrides or carbides. In addition, improving the catalytic activity by combining a highly catalytic material and a highly conductive material to form a composite material is a novel strategy.^{32–34} We attempted to design a superior catalyst, VC embedded in mesoporous carbon (VC–MC), in which MC would function as an electrical conductor and VC would function as a catalyst. As shown in Figure 2a, the broad diffraction peak at 23.6° outlined MC as it assumed an amorphous phase. The other peaks, on the other hand, can be attributed to VC, indicating that VC–MC was prepared successfully by in situ synthesis.

For the fifth-period transition metals, ZrO_2 was obtained easily, while ZrN and ZrC could not be synthesized by increasing either the urea content or the sintering temperature (Figure S2). This may be due to the fact that Zr as an element shows a strong tendency to combine with oxygen rather than nitrogen or carbon. In addition, Nb_2O_5 , NbN, and NbC(N) were synthesized without trouble at urea/metal chloride molar ratios of 1, 5, and 12, respectively (Figure S3). For Mo, unlike the other metals, MoO_2 , Mo_2N , and Mo_2C were synthesized at relatively low urea/metal chloride molar ratios of R0, R1, and R7, respectively (Figure S4). In addition, Mo_2C was obtained at

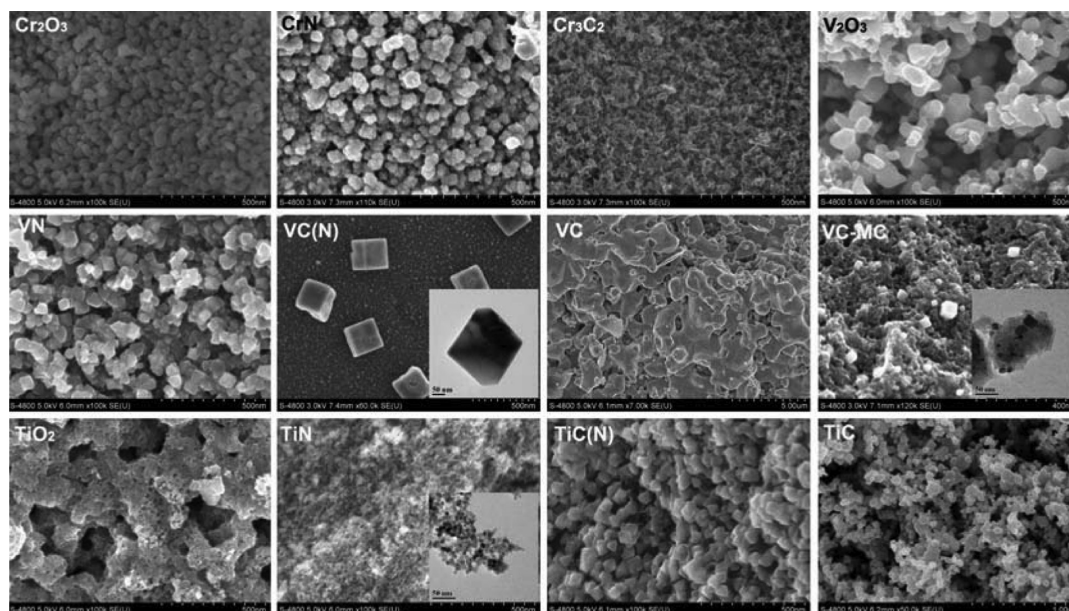


Figure 3. SEM images and (insets) TEM images of the synthesized Cr_2O_3 , CrN , Cr_3C_2 , V_2O_3 , VN , VC(N) , VC-MC , TiO_2 , TiN , and TiC(N) and commercial VC and TiC .

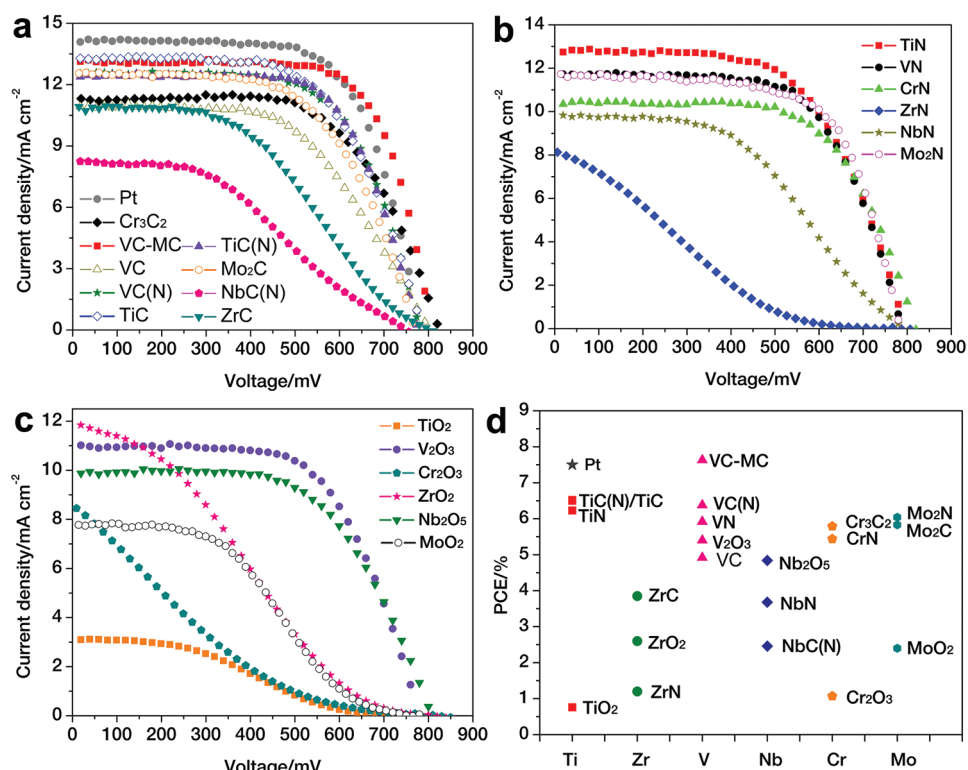


Figure 4. J - V curves for I_3^-/I^- DSCs using (a) Pt or carbide, (b) nitride, or (c) oxide CE catalysts. (d) Distribution graph showing the PCEs of these I_3^-/I^- DSCs.

relatively low sintering temperature (800 °C). The detailed experimental conditions and products are summarized in Table S2.

Figure 3 summarizes the morphologies of the Cr, V, and Ti derivatives. Cr_2O_3 existed as accumulated uniform ellipsoids with a consistent size of 30–80 nm. CrN showed an irregular nanoparticle shape, and the particle size varied from 10 to 60 nm. In fact, each irregular CrN nanoparticle was accumulated with several CrN cubes with small dimensions. The synthesized

Cr_3C_2 exhibited a network configuration constructed from Cr_3C_2 nanoparticles and had a large Brunauer–Emmett–Teller (BET) surface area of $93.8 \text{ m}^2 \text{ g}^{-1}$. In the case of V derivatives, V_2O_3 assumed a cellular structure, albeit with particles of a larger size. Both VN and VC(N) existed as well-crystallized cubes, and the cube size in VC(N) was larger than in VN . In the SEM image of VC-MC , the white cubes correspond to the VC . The inset is the corresponding TEM image, which showed that the MC exhibited a typical mesoporous structure. The

BET surface area of VC–MC was $188.0 \text{ m}^2 \text{ g}^{-1}$. The mesoporous structure can be considered as an effective electron transport network that facilitates the collection and transfer of electrons from the external circuit and subsequent regeneration of the redox couple. In addition, the network is also favorable for the mass transport of the redox couple. In contrast, the commercial VC presented large particles with irregular shapes that were interlocked with each other. For the Ti derivatives, TiO_2 also showed a typical cellular structure piled with aggregated nanoparticles. TiN assumed a typical nanoscaled cubical shape with weak aggregation, of which the diameter was approximately 10–15 nm, as shown in the inset TEM image and confirmed by the X-ray results. Meanwhile, it was evident that TiC(N) also appeared as a pile of cubes with relatively large size that adhered to one another as a result of the higher sintering temperature. The commercial TiC exhibited small cubes with diameters of 20–40 nm. The BET surface areas of TiC(N) and TiC were 57.1 and $26.7 \text{ m}^2 \text{ g}^{-1}$, respectively. The surface morphologies of MoO_3 , Mo_2N , Mo_2C , Nb_2O_5 , NbN , NbC(N) , tetragonal ZrO_2 , and monoclinic ZrO_2 are shown in Figure S5.

Photovoltaic Performance of the I_3^-/I^- DSCs using Carbide, Nitride, and Oxide CEs. Figure 4 shows the photocurrent density–voltage (J – V) curves for DSCs using Pt, carbides, nitrides, and oxides as CEs. The photovoltaic parameters are listed in Table 1. As shown in Figure 4a, the

Table 1. Photovoltaic Parameters for I_3^-/I^- DSCs Using Various CEs

CE	V_{oc} (mV)	J_{sc} (mA cm^{-2})	FF	PCE (%)
TiC(N)	778	12.50	0.67	6.52
TiC^a	788	13.30	0.62	6.50
TiN	796	12.83	0.61	6.23
TiO_2	742	3.10	0.33	0.76
VC(N)	782	12.56	0.65	6.38
VC^a	803	10.94	0.56	4.92
VN	788	11.74	0.64	5.92
V_2O_3	780	10.99	0.63	5.40
VC–MC	808	13.11	0.72	7.63
Cr_2C_3	825	11.31	0.62	5.79
CrN	818	10.39	0.64	5.44
Cr_2O_3	788	8.46	0.16	1.07
ZrC^a	803	10.91	0.44	3.85
ZrN^a	733	8.20	0.20	1.20
ZrO_2	782	11.88	0.28	2.60
NbC(N)	748	8.22	0.40	2.46
NbN	798	9.81	0.47	3.68
Nb_2O_5	808	9.98	0.60	4.84
Mo_2C	769	12.42	0.61	5.83
Mo_2N	784	11.68	0.66	6.04
MoO_2	765	7.84	0.40	2.40
Pt	783	14.08	0.68	7.50

^aThese materials were purchased.

DSCs using carbide CEs exhibited high power conversion efficiencies (PCEs) of 6.52% for TiC(N) , 6.38% for VC(N) , 5.79% for Cr_2C_3 , and 5.83% for Mo_2C . The DSCs using commercial TiC and VC CEs showed PCEs of 6.50 and 4.92%, respectively. The relatively low catalytic activity of commercial VC can be attributed to the large VC particle size, as shown in Figure 3. Some of the nitrides (Figure 4b) also gave the following high PCE values: 6.23% for TiN , 5.92% for VN ,

5.44% for CrN , and 6.04% for Mo_2N . In contrast, for the oxide CEs (Figure 4c), the DSCs using V_2O_3 and Nb_2O_5 showed just decent PCE values of 5.40 and 4.84%, respectively. For Ti , Cr , and Mo , the DSCs using carbide CEs and those using nitride CEs both exhibited high PCEs, whereas the corresponding DSCs using oxide CEs exhibited low PCEs. For V , the carbides, nitrides, and oxides all showed high catalytic activity. According to the photovoltaic performance of the Nb -based DSCs, the oxide had a higher catalytic activity than the carbide or nitride. In the case of Zr , the DSC using the ZrO_2 CE exhibited a high short-circuit current density (J_{sc}) of 11.88 mA cm^{-2} ; however, the fill factor (FF) was just 0.28, and the PCE was 2.60%. As shown in Figure 4a and Table 1, when VC–MC was used in place of VC , the J_{sc} increased from 10.94 to 13.11 mA cm^{-2} and the FF increased from 0.56 to 0.72. An extraordinarily high PCE of 7.63% was achieved on account of the superior catalytic behavior of the VC–MC CE, once again proving the feasibility of improving the catalytic activity by combining catalytic activity and electrical conductivity into one composite, as previously reported.^{32–34} By comparison, the DSC using a conventional Pt CE showed a PCE of 7.50%, which was easily matched by the VC–MC -based DSC under the same conditions. The photovoltaic results prove that a number of TMCs, TMNs, and TMOs show good catalytic activity as CE catalysts for the I_3^- reduction in DSCs. Figure 4d shows the distribution of the PCE values for the DSCs using all of the TMC, TMN, and TMO CEs. In addition, we investigated the effect of the TiC film thickness on the DSC performance and found that a thickness of $20 \mu\text{m}$ was enough to obtain an effective TiC CE (for details, see Figures S6 and S7).

For the catalytic behavior of TMCs and TMNs, the theory holds that small atoms, such as carbon or nitrogen, when inserted interstitially in the lattices of early transition metals, produce a series of TMCs or TMNs with unique physical and chemical properties. While it is evident that the electronic structure of the host metal should be modified by the alien atoms (i.e., C or N) through the electron transfer process, the direction (i.e., host metal to interstitial atom or interstitial atom to host metal) and extent of electron transfer has been debated and is discussed elsewhere.^{35–40} It is clear that the TMCs and TMNs exhibit catalytic behavior distinct from the metal hosts and that their activity patterns closely resemble those of Pt. On the other hand, why did some nitrides perform better than carbides while some carbides performed better than nitrides? As we well know, catalytic activity is one of the intrinsic characteristics of a catalyst. As pointed out above, catalytic activity is determined by the electronic structure of the catalyst. To date, however, researchers have not been able to give a definite answer concerning the electronic structure of the Pt-like catalysts and an accurate relationship between the electronic structure and the catalytic activity. In addition, for one catalyst, the catalytic activity can be also affected significantly by the particle size, crystal structure, and so forth.^{41–43} The fundamental reasons for the variety of catalytic activities of carbides, nitrides, and oxides require further studies.

Investigating the Catalytic Activities of the Carbides, Nitrides, and Oxides for the I_3^-/I^- Redox Couple by CV and EIS. To investigate the catalytic activities of the synthesized carbides, nitrides, and oxides, CV experiments were carried out. Figure 5 a–c shows typical cyclic voltammograms of various materials for the iodide species (I_3^-/I^-). For Pt, two pairs of redox peaks were observed. The pair of peaks at low potential can be attributed to the redox reaction shown in

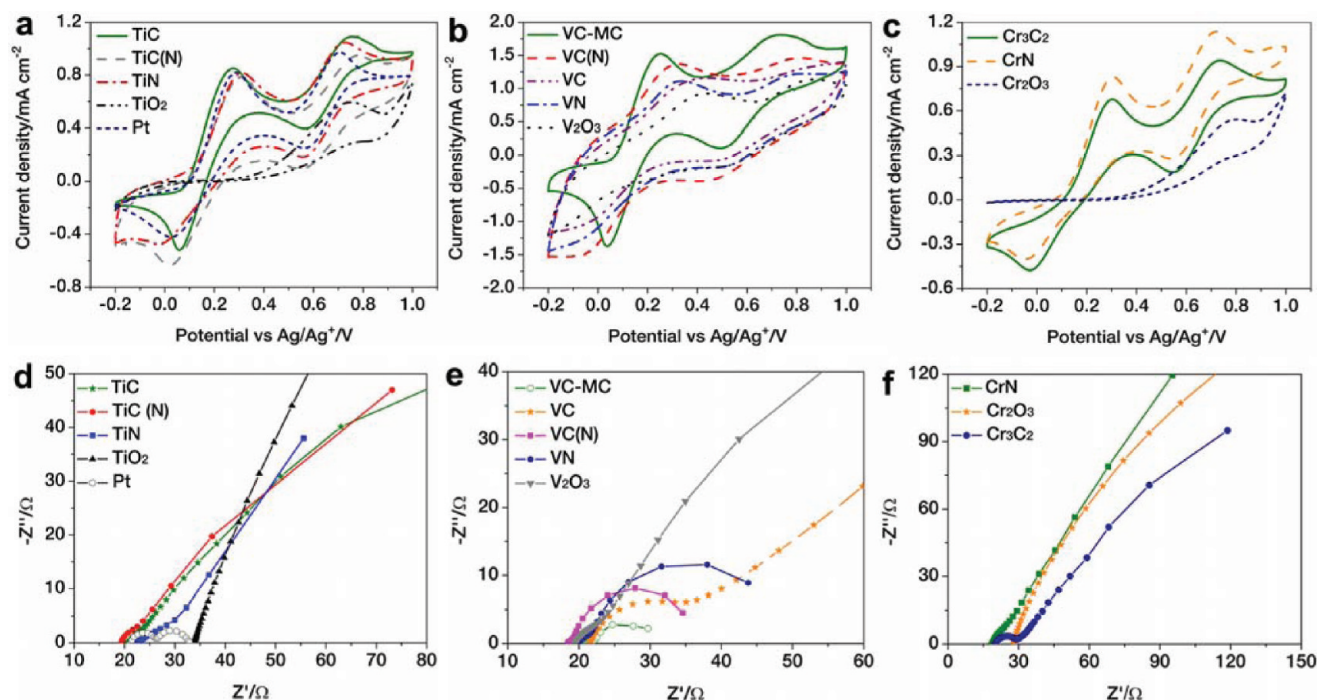
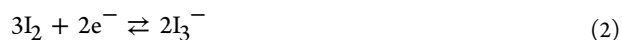


Figure 5. (a–c) Cyclic voltammograms of the (a) Ti, (b) V, and (c) Cr derivatives for I_3^-/I^- species. (d–f) Nyquist plots for the I_3^-/I^- symmetrical cells based on (d) Ti, (e) V, and (f) Cr derivative electrodes.

eq 1, and the pair at high potential can be attributed to the redox reaction shown in eq 2. TiC(N), TiC, and TiN showed two pairs of redox peaks (Figure 5a). Compared with TiN, TiC showed a relatively lower overpotential and better invertibility. This indicates the smoothness of the redox reaction of I_3^-/I^- on the TiC electrode, which produces favorable conditions for the regeneration of the sensitizer. The redox peaks of TiC at low potential (eq 1) exhibited a current density higher than that for Pt, while the redox peaks at high potential (eq 2) had a current density lower than that for Pt. On the basis of a comprehensive analysis of the potentials and current densities of the peaks, TiC and TiN both show high electrochemical catalytic activity for the reduction of I_3^- to I^- . In addition, the synthesized TiC(N) performed as effectively as the commercial TiC for the iodide species. In contrast, no redox peak was observed for TiO_2 , demonstrating lower catalytic activity. In Figure 5b, two pairs of redox peaks for VC(N), VC, VN, and V_2O_5 are visible, and the potentials of the cathodic peaks are more negative than those of the Ti derivatives. However, the current densities for the V derivatives are higher than those for the Ti derivatives on the whole. Furthermore, two pairs of redox peaks were also observed for VC–MC. In addition to the perfect appearance of the VC–MC redox peaks, the cathodic peaks moved toward positive potential while the anodic peaks moved toward negative potential relative to those for the other V derivatives. In other words, the peak-to-peak separation (ΔE_p) for VC–MC was smaller than that for the other V derivatives. In theory, ΔE_p varies inversely with charge transfer rate (k_s), and therefore, the k_s value for VC–MC can be considered the highest among the V derivatives.^{44,45} This indicates that VC–MC has better catalytic activity than the other V derivatives. This confirms again that combining the high catalytic activity of VC and good electrical conductivity of MC into one composite is a feasible method for producing a superior catalyst (VC–MC). In the case of Cr (Figure 5c), the

carbide and nitride both showed two typical pairs of redox peaks, while no obvious redox peaks were observed for Cr_2O_3 , similar to TiO_2 . Finally, for $ZrC(N)$, ZrO_2 , Nb_2O_5 , and Mo_2C , two pairs of redox peaks were observed. The cyclic voltammograms for Zr, Nb, and Mo carbides, nitrides, and oxides are summarized in the Figures S8–S10.



EIS is an effective and widely used tool for investigating the charge transfer process and thereby for evaluating the catalytic activity of a catalyst. Figure 5d–f shows Nyquist plots for the symmetrical cells fabricated with two identical Ti, V, and Cr derivative electrodes. In the case of Pt, the intercept on the real axis can generally be attributed to the series resistance (R_s). The left arch can be assigned to the charge transfer resistance (R_{ct}) and the corresponding capacitance (C_μ) of the electrode–electrolyte interface. The right arch can be assigned to the Nernst diffusion impedance (Z_N) of the redox couple (I_3^-/I^-) transport in the electrolyte. The EIS data were obtained by fitting the Nyquist plots with an equivalent circuit diagram (Figure S11), and the fit parameters are summarized in Table S3. R_{ct} was 4.7 Ω for Pt, while the R_{ct} values for TiC(N), TiC, VC(N), and VN were 6.7, 5.1, 6.2, and 9.5 Ω , respectively. This means that TiC(N), TiC, VC(N), and VN hold a high catalytic activity for I_3^- reduction. On the other hand, TiC(N), TiC, VC(N), and VN showed high Z_N relative to Pt, which might be the main factor resulting in their relatively lower catalytic activities. In contrast, TiO_2 exhibited huge R_{ct} and Z_N values, indicating poor catalytic activity. The commercial VC showed relatively large R_{ct} and Z_N values (20.8 and 350.3 Ω , respectively) due to the large particle size. V_2O_5 , however, had a low R_{ct} and Z_N in comparison with TiO_2 . As we previously reported, MC had a good electrical conductivity and

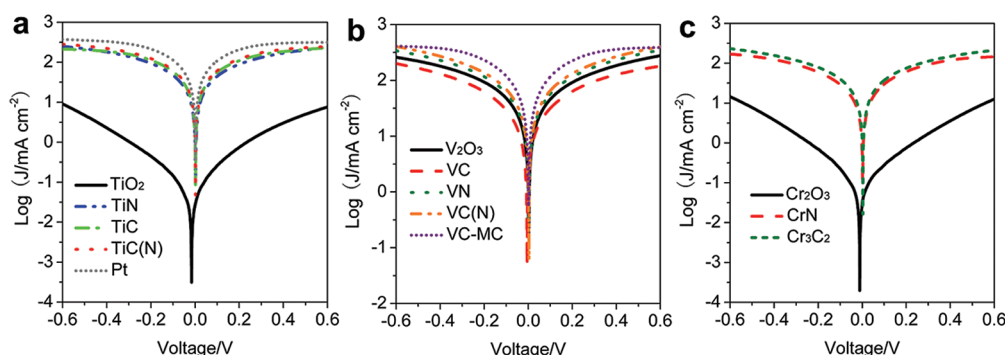


Figure 6. Tafel polarization curves of the I_3^-/I^- symmetrical cells based on (a) Ti derivatives, (b) V derivatives, and (c) Cr derivatives.

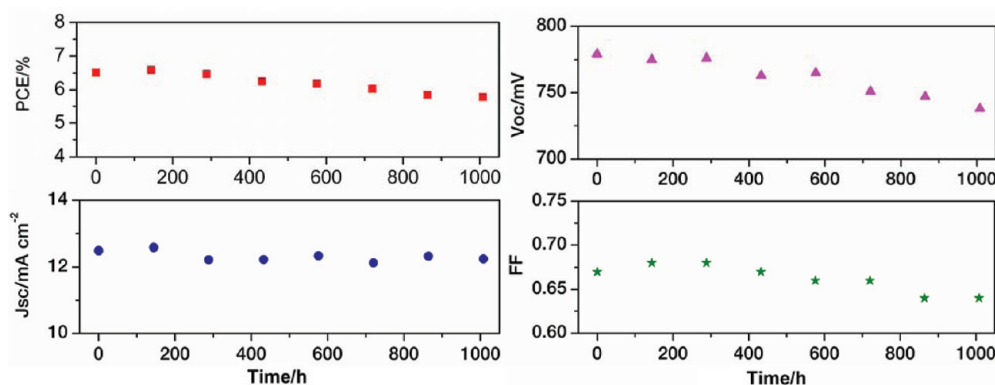


Figure 7. Stability test of the I_3^-/I^- DSC with a TiC(N) CE under natural conditions.

catalytic activity. The R_{ct} value for MC was 6.2Ω .³⁴ When VC and MC were combined, a low R_{ct} of 2.9Ω and a Z_N of 9.4Ω were obtained, both of which were lower than the corresponding values for VC(N) and VC. This can be attributed to the combined action of the high catalytic activity of VC and the high electrical conductivity of MC; this phenomenon was observed previously.^{28,32–34} In contrast, relative to VC, the R_s of VC–MC did not decline as we expected. This could stem from the poor bonding strength between the VC–MC layer and the FTO glass, leading to a large contact resistance. Furthermore, VC–MC had a huge C_{μ} , reflecting a large surface area ($188.0 \text{ m}^2 \text{ g}^{-1}$). This large surface area corresponds to the formed mesoporous network, a curtail issue for high catalytic activity. The R_{ct} values for Cr_3C_2 , Mo_2C , and Mo_2N were all $<10 \Omega$, resulting in high catalytic activity, whereas Cr_2O_3 and ZrN both had R_{ct} larger than 400Ω , producing poor catalytic activity. The R_{ct} values for ZrC , ZrO_2 , NbC(N) , NbN , Nb_2O_5 , and MoO_2 were in the range of 20–200 Ω . The Nyquist plots of Zr, Nb, and Mo derivative-based symmetrical cells are shown in Figures S12–S14, and the corresponding fit parameters are summarized in Table S3.

Polarization Tests of the Carbides, Nitrides, and Oxides for the I_3^-/I^- Redox Couple. Tafel polarization measurements were used to reconfirm the catalytic activity of the novel carbide, nitride, and oxide electrodes. Figure 6 shows the Tafel curves for symmetrical cells similar to the ones used in the EIS measurements. The curves show logarithmic current density (J) as a function of voltage (V) (Detailed Tafel polarization analysis can be found in Figure S15). In Figure 6a, the curves of the TiC(N), TiC, and TiN exhibited a large exchange current density (J_0) in comparison with that of the Pt electrode. This means that TiC(N), TiC, and TiN have

superior catalytic activity for I_3^- reduction. In contrast, the curve for TiO_2 showed a lower J_0 , demonstrating that TiO_2 cannot perform as effectively as TiC or TiN. The equilibrium potential departed from the location of zero potential, which might be caused by absorption of I_3^- on the TiO_2 surface, inducing an interruption in the redox reaction between I_3^- and I^- , or by a high scan rate. In the CV test, the absence of the cathodic peaks of TiO_2 can be attributed to the same reasons. On the other hand, TiC(N), TiC, and TiN showed a high limiting diffusion current density (J_{lim}) relative to that of Pt, reflecting a higher diffusion velocity for the redox couple in the electrolyte. In Figure 6b, VC(N), VC, VN, and V_2O_5 all showed decent J_0 and J_{lim} values. When VC was embedded in MC, J_0 was improved significantly in comparison with VC. In the case of Cr, Cr_3C_2 and CrN showed high J_0 and J_{lim} , and Cr_2O_3 performed the worst (Figure 6c). In theory, J_0 varies inversely with R_{ct} (eq S1 in the Supporting Information). With the EIS results, the change tendency of J_0 for various electrodes is generally in accordance with those presented in the Tafel curve plots. J_{lim} is determined by the diffusion properties of the redox couple and the CE catalysts; at the same potential, a large J_{lim} indicates a large diffusion coefficient and a small Z_N (eqs S2 and S3). After performing a comprehensive analysis of the EIS and Tafel polarization results, we conclude that the photovoltaic performance is in agreement with the EIS and Tafel polarization results on the whole.

Long-Term Stability Tests of the I_3^-/I^- DSCs. An excellent catalyst should contain two fundamental characteristics: high catalytic activity and perfect stability. Pt exhibits high catalytic activity, and Pt-based DSCs always show good stability. However, for Pt- and I_3^-/I^- -based DSCs, Olsen et al.⁴⁶ found that Pt may be dissolved in the electrolyte containing the

I_3^-/I^- redox couple, producing PtI_4 . Hauch et al.⁴⁷ also found that Pt can be contaminated by components in the air. In this work, a long-term stability test of the DSC using the TiC(N) CE was carried out under natural conditions. As shown in Figure 7, after 1000 h, the photovoltaic parameters of open-circuit voltage (V_{oc}), J_{sc} , FF, and PCE retained 95, 98, 96, and 89% of their initial values, respectively. The high stability of the DSC can be attributed to the fact that TMCs possess intrinsic excellent corrosion resistance and perfect stability. In addition, under illumination, another long-term stability test was performed, this one using the DSC with the TiC CE and a 3-methoxypropionitrile (MPN)-based electrolyte. After 6 months, the PCE of the DSC decreased from 6.4 to 5.0%; we will report this specific stability measurement elsewhere. The excellent stability of carbides and nitrides under harsh conditions is one of their intrinsic merits and this makes them more suitable for low-cost and long-term-stable DSCs.

Application of the Carbides with a New Organic Redox Couple (T_2/T^-). In addition, we introduced the carbides of TiC, VC, VC-MC, and Cr_3C_2 into a new organic redox couple (T_2/T^-).⁹ Figure 8 shows that the traditional Pt

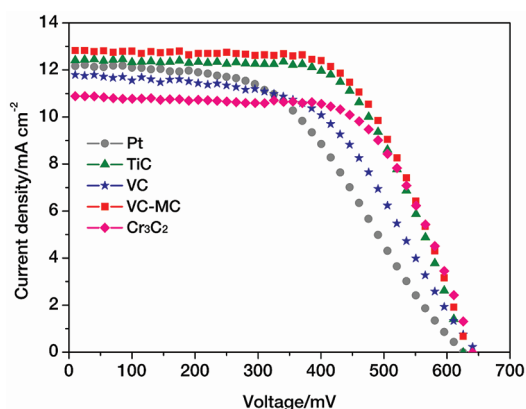


Figure 8. J - V curves for the T_2/T^- DSCs using TiC, VC, VC-MC, Cr_3C_2 , and Pt CEs.

CE exhibited depressed catalytic behavior for the reduction of T_2 to T^- , and the DSC yielded a low PCE of 3.66% (V_{oc} , 625 mV; J_{sc} , 12.23 $mA\ cm^{-2}$; FF, 0.48). In contrast, all of the carbide CEs brought clear advantages to the T_2/T^- system. The DSCs using TiC, VC, VC-MC, and Cr_3C_2 CEs showed high PCEs of 4.96, 4.06, 5.15, and 4.54%. The PCE values were significantly improved to 35.5, 10.9, 40.7, and 24.4%, respectively. The photovoltaic parameters are summarized in Table S4. We can say that the carbides displayed higher suitability for the T_2/T^- redox couple than the I_3^-/I^- redox couple. To check the catalytic activities of carbides and Pt for the reduction of T_2 to T^- , CV and EIS experiments were carried out as discussed below.

Figure 9 shows the cyclic voltammograms of the carbide and Pt CEs with the T_2/T^- redox couple. One pair of redox peaks was observed for all of the electrodes. In the case of Pt, the redox peaks appeared at -0.41 and 0.49 V, and the ΔE_p was 0.90 V. In contrast, the redox peaks for TiC appeared at -0.24 and 0.31 V, giving a ΔE_p of 0.55 V. As discussed above, ΔE_p varies inversely with k_s . Thus, TiC has a larger k_s than Pt, which is favorable for high catalytic activity. In addition, the cathodic current densities of the carbide electrodes were higher than that of Pt. The CV results indicate that the carbide electrodes

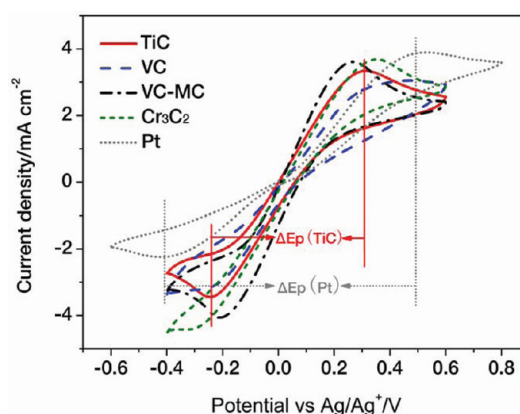


Figure 9. Cyclic voltammograms of the carbides and Pt electrodes for T_2/T^- redox species in a three-electrode system in an argon-purged acetonitrile solution containing 100 mM $Me_4N^+T^-$, 10 mM T_2 , and 0.2 M $LiClO_4$ measured at a scan rate of $10\ mV\ s^{-1}$. Pt served as the CE and Ag/Ag^+ as the reference electrode.

perform better than Pt for the regeneration of the T_2/T^- redox couple. Figure S16 showed that after 10 cycles, no current density decline and peak shifts were observed for the TiC electrode. This demonstrates that TiC and T_2/T^- species can coexist long-term.¹⁹ Finally, EIS measurements were also carried out to check the catalytic activities of the carbides for the T_2/T^- redox couple. As shown in Figure 10, the R_{ct} value of

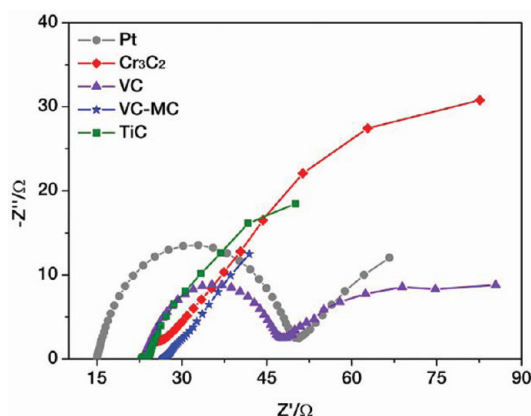


Figure 10. Nyquist plots for the T_2/T^- symmetrical cells based on carbides and Pt electrodes.

the symmetrical cell based on the Pt CE and the T_2/T^- electrolyte was $35.1\ \Omega$, whereas the R_{ct} values for TiC, VC, VC-MC, and Cr_3C_2 (5.1 , 24.9 , 4.8 , and $14.0\ \Omega$, respectively) were much lower. This is the main reason for the higher photovoltaic performance of the DSCs using carbide CEs. The EIS parameters are summarized in Table S4.

Very recently, we used TiC and Pt in Co^{3+}/Co^{2+} electrolyte-based DSCs and obtained PCEs of 4.13 and 2.91%, respectively. Future works will provide more details and elaborate on this study. We found that similar to semiconductors and sensitizers, there existed a fit issue between the CE catalysts and redox couples. Pt-free catalysts may be more suitable for iodide-free redox couples. More attention should be paid to this issue in the process of developing new CE catalysts as well as new redox couples.

■ CONCLUSION

Three distinct groups of materials were synthesized and applied into DSC systems as counter electrode catalysts: IVB, VB, and VIB transition-metal (1) carbides, (2) nitrides, and (3) oxides. Of these materials, TiC, TiC(N), VC(N), VC, Cr₃C₂, Mo₂C, TiN, VN, Mo₂N, V₂O₃, and Nb₂O₅ showed high catalytic activity for triiodide reduction in DSC systems. The catalytic activity was improved significantly by combining both high catalytic activity (VC) and high electrical conductivity (MC) into the composite material VC–MC. Remarkable stability due to the intrinsic corrosion resistance of the carbides was achieved. These achievements, in turn, provide the possibility of industrializing DSCs by using low-cost transition metal carbides, nitrides, and oxides as CE catalysts. In addition, the carbides performed better than Pt in catalyzing the reduction of T₂ to T[−]. The TMCs, TMNs, and TMOs may be also suitable for the regeneration of the Co³⁺/Co²⁺ redox couple; work on this is in progress. The fit between the properties of the CE catalyst and the characteristics of the redox couple should be considered in the development of low-cost, high-efficiency DSCs in future studies.

■ ASSOCIATED CONTENT

■ Supporting Information

XPS spectrum of TiC(N) (Figure S1); XRD patterns of Zr, Nb, Mo derivatives (Figures S2–S4); SEM images of the surface morphologies of MoO₃, Mo₂N, Mo₂C, Nb₂O₅, NbN, NbC(N), tetragonal ZrO₂, and monoclinic ZrO₂ (Figure S5); SEM images of TiC films with different thicknesses (Figure S6); *J*–*V* curves for the DSCs based on TiC CEs with different thicknesses (Figure S7); cyclic voltammograms for Zr, Nb, and Mo derivatives (Figures S8–S10), equivalent circuit diagram (Figure S11); Nyquist plots for symmetrical cells based on Zr, Nb, and Mo derivative electrodes (Figures S12–S14), details of Tafel polarization analysis (Figure S15); 10 consecutive cyclic voltammograms of the TiC electrode for T₂/T[−] (Figure S16); synthesis details and characteristics of the products (Tables S1 and S2); EIS parameters of the I₃[−]/I[−] symmetrical cells (Table S3); and photovoltaic parameters of the T₂/T[−] DSCs and EIS parameters of the T₂/T[−] symmetrical cells (Table S4). This material is available free of charge via the Internet at <http://pubs.acs.org>.

■ AUTHOR INFORMATION

Corresponding Author

tinglima@dlut.edu.cn; Pengxj@dlut.edu.cn

■ ACKNOWLEDGMENTS

This research was supported by the National Natural Science Foundation of China (Grant 50773008), the State Key Laboratory of Fine Chemicals of China, and the National High Technology Research and Development Program for Advanced Materials of China (Grant 2009AA03Z220).

■ REFERENCES

- (1) O'Regan, B.; Grätzel, M. *Nature* **1991**, *353*, 737–740.
- (2) Grätzel, M. *Nature* **2001**, *414*, 338–344.
- (3) Hagfeldt, A.; Boschloo, G.; Sun, L.; Kloo, L.; Pettersson, H. *Chem. Rev.* **2010**, *110*, 6595–6663.
- (4) Fang, X. M.; Ma, T. L.; Guan, G. Q.; Akiyama, M.; Kida, T.; Abe, E. *J. Electroanal. Chem.* **2004**, *570*, 257–263.
- (5) Ma, T. L.; Fang, X. M.; Akiyama, M.; Inoue, K.; Noma, H.; Abe, E. *J. Electroanal. Chem.* **2004**, *574*, 77–83.

- (6) Li, P.; Wu, J.; Lin, J.; Huang, M.; Lan, Z.; Li, Q. *Electrochim. Acta* **2008**, *53*, 4161–4166.
- (7) Calogero, G.; Calandra, P.; Irrera, A.; Sinopoli, A.; Citro, I.; Di Marco, G. *Energy Environ. Sci.* **2011**, *4*, 1838–1844.
- (8) Wang, L.; Wu, M. X.; Gao, Y. R.; Ma, T. L. *Appl. Phys. Lett.* **2011**, *98*, No. 221102.
- (9) Wang, M. K.; Chamberland, N.; Breau, J.; Moser, J.-E.; Humphry-Baker, R.; Marsan, B.; Zakeeruddin, S. M.; Grätzel, M. *Nat. Chem.* **2010**, *2*, 385–389.
- (10) Feldt, S. M.; Gibson, E. A.; Gabrielsson, E.; Sun, L.; Boschloo, G.; Hagfeldt, A. *J. Am. Chem. Soc.* **2010**, *132*, 16714–16724.
- (11) Yella, A.; Lee, H.-W.; Tsao, H. N.; Yi, C.; Chandiran, A. K.; Nazeeruddin, M. K.; Diau, E. W.-G.; Yeh, C.-Y.; Zakeeruddin, S. M.; Grätzel, M. *Science* **2011**, *334*, 629–634.
- (12) Bashyam, E.; Zelenay, P. *Nature* **2006**, *443*, 63–66.
- (13) Kay, A.; Grätzel, M. *Sol. Energy Mater. Sol. Cells* **1996**, *44*, 99–117.
- (14) Wu, M. X.; Lin, X.; Wang, T. H.; Qiu, J. S.; Ma, T. L. *Energy Environ. Sci.* **2011**, *4*, 2308–2315.
- (15) Roy-Mayhew, J. D.; Bozym, D. J.; Punckt, C.; Aksay, I. A. *ACS Nano* **2010**, *4*, 6203–6211.
- (16) Lee, K. M.; Hsu, C. Y.; Chen, P. Y.; Ikegami, M.; Miyasaka, T.; Ho, K. C. *Phys. Chem. Chem. Phys.* **2009**, *11*, 3375–3379.
- (17) Tai, Q.; Chen, B.; Guo, F.; Xu, S.; Hu, H.; Sebo, B.; Zhao, X.-Z. *ACS Nano* **2011**, *5*, 3795–3799.
- (18) Wang, M. K.; Anghel, A. M.; Marsan, B.; Ha, N. C.; Pootrakulchote, N.; Zakeeruddin, S. M.; Grätzel, M. *J. Am. Chem. Soc.* **2009**, *131*, 15976–15977.
- (19) Sun, H.; Qin, D.; Huang, S.; Guo, X.; Li, D.; Luo, Y.; Meng, Q. *Energy Environ. Sci.* **2011**, *4*, 2630–2637.
- (20) Jiang, Q. W.; Li, G. R.; Liu, S.; Gao, X. P. *J. Phys. Chem. C* **2010**, *114*, 13397–13401.
- (21) Hwu, H. H.; Chen, J. G. *Chem. Rev.* **2005**, *105*, 185–212.
- (22) Levy, R. B.; Boudart, M. *Science* **1973**, *181*, 547–549.
- (23) Rodrigues, J. A. J.; Cruz, G. M.; Bugli, G.; Boudart, M.; Djéga-Maridassou, G. *Catal. Lett.* **1997**, *45*, 1–3.
- (24) Hara, Y.; Minami, N.; Matsumoto, H.; Itagaki, H. *Appl. Catal., A* **2007**, *332*, 289–296.
- (25) Ganesan, R.; Lee, J. S. *Angew. Chem., Int. Ed.* **2005**, *44*, 6557–6560.
- (26) Tomchenko, A. A.; Emelianov, I. L.; Khatko, V. V. *Sens. Actuators, B* **1999**, *57*, 166–170.
- (27) Liu, F.; Li, L.; Mo, F.; Chen, J.; Deng, S.; Xu, N. *Cryst. Growth Des.* **2010**, *10*, S193–S199.
- (28) Wu, M. X.; Lin, X.; Hagfeldt, A.; Ma, T. L. *Angew. Chem., Int. Ed.* **2011**, *50*, 3520–3524.
- (29) Wu, M. X.; Lin, X.; Hagfeldt, A.; Ma, T. L. *Chem. Commun.* **2011**, *47*, 4535–4537.
- (30) Jang, J.; Ham, D.; Ramasamy, E.; Lee, J.; Lee, J. S. *Chem. Commun.* **2010**, *46*, 8600–8602.
- (31) Giordano, G.; Erpen, C.; Yao, W.; Milke, B.; Antonietti, M. *Chem. Mater.* **2009**, *21*, S136–S144.
- (32) Li, G. R.; Wang, F.; Jiang, Q. W.; Gao, X. P.; Shen, P. W. *Angew. Chem., Int. Ed.* **2010**, *49*, 3653–3656.
- (33) Sudhagar, P.; Nagarajan, S.; Lee, Y.-G.; Song, D.; Son, T.; Cho, W.; Heo, M.; Lee, K.; Won, J.; Kang, Y. S. *ACS Appl. Mater. Interfaces* **2011**, *3*, 1838–1843.
- (34) Wu, M. X.; Lin, X.; Wang, L.; Wang, Y. D.; Xiao, J. Q.; Hagfeldt, A.; Ma, T. *J. Phys. Chem. C* **2011**, *115*, 22598–22602.
- (35) Alexander, A.-M.; Hargreaves, J. S. J. *Chem. Soc. Rev.* **2010**, *39*, 4388–4401.
- (36) Bennett, L. H.; Cuthill, J. R.; McAlister, A. J.; Erickson, N. E. *Science* **1974**, *184*, 563–565.
- (37) Houston, J. E.; Laramore, G. E.; Park, R. L. *Science* **1974**, *185*, 258–259.
- (38) Bennett, L. H.; Cuthill, J. R.; McAlister, A. J.; Erickson, N. E. *Science* **1975**, *187*, 858–859.
- (39) Kitchin, J. R.; Nørskov, J. K.; Barteau, M. A.; Chen, J. G. *Catal. Today* **2005**, *105*, 66–73.

- (40) Oyama, S. T. *Catal. Today* **1992**, *15*, 179–200.
- (41) Ramasamy, E.; Lee, W. J.; Lee, D. Y.; Song, J. S. *Appl. Phys. Lett.* **2007**, *90*, No. 173103.
- (42) Lin, X.; Wu, M. X.; Wang, Y. D.; Hagfeldt, A.; Ma, T. L. *Chem. Commun.* **2011**, *47*, 11489–11491.
- (43) Ko, A.-R.; Oh, J.-K.; Lee, Y.-W.; Han, S.-B.; Park, K.-W. *Mater. Lett.* **2011**, *65*, 2220–2223.
- (44) Ramasamy, E.; Lee, J. *Carbon* **2010**, *48*, 3715–3720.
- (45) Nicholson, R. S. *Anal. Chem.* **1965**, *37*, 1351–1355.
- (46) Olsen, E.; Hagen, G.; Lindquist, S. E. *Sol. Energy Mater. Sol. Cells* **2000**, *63*, 267–273.
- (47) Hauch, A.; Georg, A. *Electrochim. Acta* **2001**, *46*, 3457–3466.